

# Design of a Split Ring Resonator Integrated with On-Chip Terahertz Waveguides for Colon Cancer Detection

Sae June Park,\* Robyn Tucker, Emma Pickwell-MacPherson, and John E. Cunningham\*

Finite element method (FEM) simulations (employing ANSYS High Frequency Structure Simulator, HFSS) are used to investigate the response of terahertz (THz) frequency range split-ring resonators (SRRs) integrated with on-chip THz waveguides to cancerous tissues. Two-port S-parameter simulations are performed to obtain the transmission spectra ( $S_{21}$ ) of a planar Goubau line (PGL) integrated with an SRR. Permittivity and loss tangent of the colonic tissues are both taken into account in the numerical simulation. The transmission spectra of the SRR integrated PGL are obtained for cancerous and healthy tissues in close proximity to the SRR, and it is found that they can be distinguished by the resonant frequency shift of the SRR induced by dielectric loading. The electric field distribution and magnitude near the SRR for various capacitive gap widths of SRR are investigated to understand how the gap width affects the maximum electric field magnitude and the vertical extent of the electric field in the gap area. The simulated imaging of colonic tissue consisting of healthy and cancerous tissues using the SRR integrated PGL device with a protective layer on it is performed, showing how the technique could in principle be used to distinguish tumor margins with realistic THz dielectric parameters.

Pre-screening of CRC in asymptomatic patients is an effective way to reduce cancer risk as cancer survival rates improve significantly when cancer is diagnosed and treated early.<sup>[2]</sup> Colonoscopy has been considered the gold standard of CRC detection as it allows colorectal surgeons to have a detailed look at the entire colon.<sup>[3,4]</sup> However, colonoscopy adenoma miss rates, varying between 6% and 27% have been reported by several studies.<sup>[4]</sup> This imprecision makes developing novel in vivo detection methods that can be integrated into existing colonoscopy probes very timely.

Various studies have proposed the use of free-space THz spectroscopy to image cancerous tissues drawing upon its non-contact,<sup>[5]</sup> and non-ionizing<sup>[6]</sup> properties. Imaging of skin cancer has been receiving particular attention owing to its easily accessible location on the human skin which is not restricted by the limited tissue penetration depth of THz radiation.<sup>[6]</sup> Reid et al. (2011) reported, for example, that freshly excised cancerous colonic

tissue can be differentiated from healthy tissue using THz spectroscopy.<sup>[2]</sup> It has also been reported that subcutaneous cancers can be detected using THz imaging.<sup>[7]</sup> For most other in vivo applications (e.g., CRC detection), however, the limited tissue penetration depth makes free-space THz imaging of cancer challenging.<sup>[6]</sup>

On-chip THz spectroscopy provides a compact<sup>[8]</sup> and planar geometry<sup>[9]</sup> that can potentially be integrated into the existing colonoscopy probes. We recently showed that SRRs-integrated with on-chip THz waveguides can be used to detect target dielectric materials deposited on the chip, and the permittivity of unknown analytes determined at multiple frequencies.<sup>[10]</sup> Such systems could offer an ideal platform to examine target tissues inside the human body (e.g., in the colon) owing to their compactness<sup>[8]</sup> and good sensitivity to the water content.<sup>[11]</sup> Various geometrical parameters in SRR and on-chip THz waveguides can be adjusted to optimize the performance of the chip depending on the applications.<sup>[10,12]</sup> Therefore, it is timely to explore methods to that could perform imaging of cancers with SRR integrated on-chip THz waveguides in order to maximize the detection sensitivity.

In this work, we perform FEM simulations of SRRs integrated on-chip THz waveguides to investigate their utility for in vivo CRC imaging. SRR integrated PGL and colonic tissues were modeled in the simulation to investigate how healthy and


## 1. Introduction

Colorectal cancer (CRC) was the second leading cause of death worldwide in 2020, with  $\approx 935\,173$  deaths estimated.<sup>[1]</sup>

S. J. Park  
School of Electronic Engineering and Computer Science  
Queen Mary University of London  
London E1 4NS, UK  
E-mail: s.j.park@qmul.ac.uk

R. Tucker, J. E. Cunningham  
School of Electronic and Electrical Engineering  
University of Leeds  
Leeds LS2 9JT, UK  
E-mail: j.e.cunningham@leeds.ac.uk

E. Pickwell-MacPherson  
Department of Physics  
University of Warwick  
Coventry CV41 7AL, UK

 The ORCID identification number(s) for the author(s) of this article can be found under <https://doi.org/10.1002/adts.202200313>

© 2022 The Authors. Advanced Theory and Simulations published by Wiley-VCH GmbH. This is an open access article under the terms of the Creative Commons Attribution License, which permits use, distribution and reproduction in any medium, provided the original work is properly cited.

DOI: 10.1002/adts.202200313

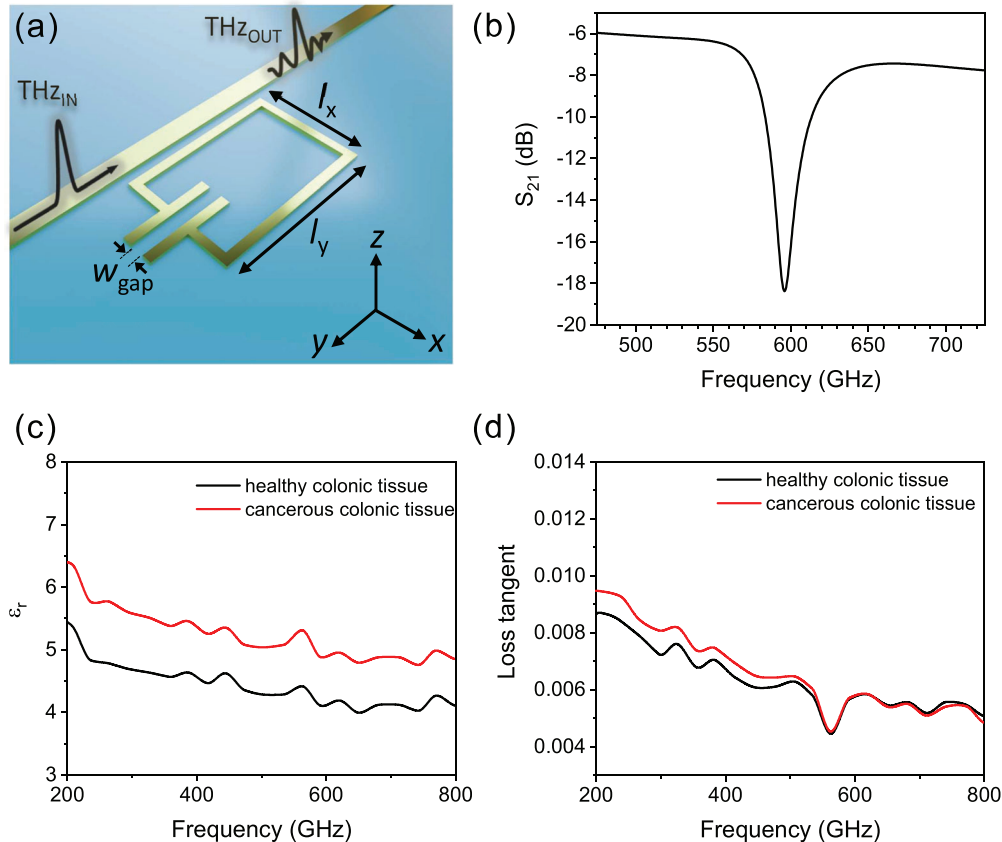


**Figure 1.** a) Schematic of the SRR integrated PGL model used in the simulations. b) The calculated transmission parameter  $S_{21}$  of the SRR integrated PGL. c) Real permittivity and d) loss tangent of healthy and cancerous colonic tissues in the THz frequency range.<sup>[2]</sup>

cancerous colon tissues can be distinguished from each other using their THz response. The instantaneous electric field distribution near the SRR on resonance was explored for various capacitive gap widths to find optimal geometrical parameters for this imaging application. Specifically, a tissue consisting of healthy and cancerous tissue was examined using an SRR integrated with PGL with a protective layer on it, the latter to ensure biological compatibility.

## 2. Simulation Method

To obtain  $S_{21}$  of the SRR integrated PGL on a quartz substrate, we used ANSYS High-Frequency Structure Simulator (HFSS). **Figure 1a** shows a part of 5  $\mu\text{m}$ -wide, 500  $\mu\text{m}$ -long PGL with an SRR consisting of a rectangular ring with outer dimensions of  $l_x \times l_y$  with a line width of 2  $\mu\text{m}$  and a capacitive gap structure with a gap width of  $w_{\text{gap}}$ . The gap between PGL and the SRR was 2  $\mu\text{m}$ . A 100  $\mu\text{m}$ -thick quartz substrate was used with a permittivity of 3.8, which is valid in the frequency range of 50–1100 GHz.<sup>[13]</sup> Both the PGL and SRR have a metal thickness of 150 nm which is larger than THz skin depth of gold at 500 GHz.  $w_{\text{gap}}$  was chosen in the range of 1–10  $\mu\text{m}$ , while  $l_x$  and  $l_y$  were 25 and 40  $\mu\text{m}$  respectively.  $S_{21}$  of the SRR integrated PGL was obtained by performing two-port S-parameter simulations. Wave-ports were directly coupled to the PGL to generate and detect THz signals. To prevent any incident electric and magnetic fields on the boundaries, a ra-

diation boundary condition was chosen in the simulation model. **Figure 1b** shows the simulated  $S_{21}$  of the SRR integrated with PGL when  $w_{\text{gap}} = 4 \mu\text{m}$ , showing a single inductive-capacitive (LC) resonance at 596 GHz ( $f_0$ ).

For the simulations of colonic tissue, three types of tissue models were designed. Tissue model I: a healthy colonic tissue with a thickness of  $h_{\text{tissue}}$ , a width of 170  $\mu\text{m}$ , and a length of 170  $\mu\text{m}$ . Tissue model II: a cancerous colonic tissue block with a thickness of  $h_{\text{tissue}}$ , a width of 170  $\mu\text{m}$ , and a length of 170  $\mu\text{m}$ . Tissue model III: a healthy colonic tissue block with a thickness of 20  $\mu\text{m}$ , a width of 170  $\mu\text{m}$ , and a length of 170  $\mu\text{m}$  part with a cylindrical cancerous colonic tissue of radius 140  $\mu\text{m}$  in the middle. We note that geometrical parameters used in the simulations are tabulated in **Table 1**. Real permittivity and the loss tangent of healthy and cancerous colonic tissues used in the simulations are shown in **Figure 1c,d**, respectively. These dielectric properties were extracted and reproduced from the experimental work by Reid et al. (2011).<sup>[2]</sup> We note that cancerous colonic tissue has a higher real permittivity value across the broadband THz frequency range from 0.2–0.8 THz. Cancerous and healthy colonic tissues have permittivity values of 4.90 and 4.13 at the operating frequency of the SRR ( $f_0 = 596 \text{ GHz}$ ), respectively, while they have the same loss tangent of 0.0057 at  $f_0$ . We note that, as previously reported,<sup>[10]</sup> the loss tangent value of the target material does not significantly affect the resonant frequency shift of the SRR, so weak resonances in loss tangent such as that

**Table 1.** Geometrical parameters used for modelling of SRR integrated on-chip waveguides.

Substrate thickness	100 $\mu\text{m}$	Gap between SRR and PGL	2 $\mu\text{m}$
PGL length	500 $\mu\text{m}$	Metal thickness	150 nm
PGL width	5 $\mu\text{m}$	SRR line width	2 $\mu\text{m}$
Width of SRR	25 $\mu\text{m}$	Tissue thickness	20 $\mu\text{m}$
Length of SRR	40 $\mu\text{m}$	Tissue length	170 $\mu\text{m}$
Capacitive gap width	1–10 $\mu\text{m}$	Tissue width	170 $\mu\text{m}$
Capacitive gap length	20 $\mu\text{m}$	Polyimide layer thickness	1 $\mu\text{m}$

seen at 550 GHz in the experimental data should not affect our conclusions.

### 3. Simulation Results and Discussion

To study how healthy and cancerous colonic tissues can be differentiated from each other using the SRR integrated PGL, Tissue model I (healthy colonic tissue) and II (cancerous colonic tissue) were located on the SRR with  $w_{\text{gap}} = 4 \mu\text{m}$ . **Figure 2a,b** shows a diagram of the SRR integrated PGL with Tissue model I, and II overlaid on top respectively. The center of the tissue models was located in the center of the gap structure of the SRR. **Figure 2c** shows the simulated  $S_{21}$  of the SRR with Tissue model I, and Tissue model II when  $h_{\text{tissue}} = 20 \mu\text{m}$ , and without the tissue models. The LC resonance of the SRR without loading of tissue layer can be described by following equation:  $f_0 = 1/2\pi\sqrt{LC}$ , where  $L$  is the inductance of the side arm ring of the SRR, and  $C$  is the capacitance in the gap area.<sup>[14]</sup> The LC resonance ( $f$ ) upon loading of the tissue can be expressed by  $f = f_0(\epsilon/\epsilon_{\text{eff}})^{-1/2}$ , where  $\epsilon$  and  $\epsilon_{\text{eff}}$  are the effective permittivities near the SRR with and without the tissue loading, respectively.<sup>[15]</sup> The resonant frequency shift was 130 and 155 GHz when Tissue model I and II was located on the device, respectively, showing that healthy and cancerous colonic tissues can be distinguished from each other by comparing the size of the resonant frequency shift. The resonant frequency shift of

the SRR as a function of  $h_{\text{tissue}}$  was also investigated in **Figure 2d**. The difference in the resonant frequency shift between Tissue model I and II cases increases up to 25 GHz as  $h_{\text{tissue}}$  increases, but no longer changes when  $h_{\text{tissue}} > 10 \mu\text{m}$ . We note that the SRR integrated PGL still can distinguish the healthy and cancerous colonic tissues when  $h_{\text{tissue}} < 10 \mu\text{m}$ , while the maximum sensitivity for the distinction can be achieved when  $h_{\text{tissue}} > 10 \mu\text{m}$ .

The sensitivity for the dielectric sensing and the effective sensing height of the SRR structure are mainly determined by  $w_{\text{gap}}$ .<sup>[16]</sup> Therefore, we investigated the effect of  $w_{\text{gap}}$  on the electric field confinement and distribution, and the magnitude of the instantaneous electric field near the gap structure at the operating frequency of the SRR for  $w_{\text{gap}}$  in the range of 1–10  $\mu\text{m}$ . **Figure 3a,b** shows the field confinement and distribution along the  $z$ - $x$  plane for  $w_{\text{gap}} = 1 \mu\text{m}$ , and  $w_{\text{gap}} = 10 \mu\text{m}$ , respectively. We first defined an area containing electric field strengths within one order of magnitude of the maximum electric field strength as the area of field confinement (see the dotted orange lines, **Figure 3a,b**). We obtained the confinement areas of 6 and 111  $\mu\text{m}^2$  for the SRRs with  $w_{\text{gap}} = 1$ , and 10  $\mu\text{m}$ , respectively. The SRR with  $w_{\text{gap}} = 1 \mu\text{m}$  shows  $\approx 18$  times more confined electric field distribution compared to the SRR with  $w_{\text{gap}} = 10 \mu\text{m}$ . In **Figure 3c**, the electric field magnitude was plotted at the center of the gap structure as a function of the vertical position ( $z$ ) for  $w_{\text{gap}} = 1, 2, 5, 10 \mu\text{m}$ . **Figure 3d** shows the maximum electric field magnitude (at  $z = 0 \mu\text{m}$ ) at the center of the gap structure as a function of  $w_{\text{gap}}$  in the range 1–10  $\mu\text{m}$ . The maximum magnitude of the field for the SRR with  $w_{\text{gap}} = 1 \mu\text{m}$  is  $\approx 5.6 \times 10^7 \text{ V m}^{-1}$  which is  $\approx 28$  times stronger than that of the SRR with  $w_{\text{gap}} = 10 \mu\text{m}$  ( $2 \times 10^6 \text{ V m}^{-1}$ ). On the other hand, the decay length of the electric field magnitude obtained by an exponential fit in the air ( $z > 0 \mu\text{m}$ ) was plotted as a function of  $w_{\text{gap}}$  in **Figure 3e**. The decay length (effective sensing height) increases  $\approx 5$  times from 1.3  $\mu\text{m}$  ( $w_{\text{gap}} = 1 \mu\text{m}$ ) to 6.4  $\mu\text{m}$  ( $w_{\text{gap}} = 10 \mu\text{m}$ ). These results indicate that reducing  $w_{\text{gap}}$  increases the electric field magnitude in the gap area of the SRR, leading to greater sensitivity,<sup>[17]</sup> while the effective sensing height decreases with decreasing  $w_{\text{gap}}$ .<sup>[16]</sup> We note that these criteria should be considered when designing practical implementations of an SRR with integrated on-chip THz waveguide probes.

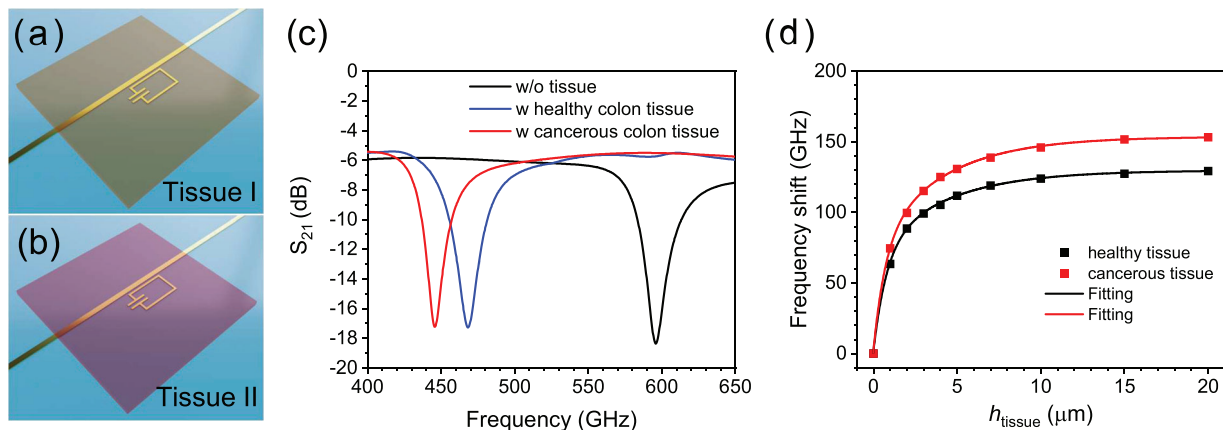


**Figure 2.** Schematics of the SRR integrated PGL model with a) healthy colonic tissue (Tissue model I) and b) cancerous colonic tissue (Tissue model II). c)  $S_{21}$  parameter of the SRR without tissue (black line), with healthy colonic tissue (blue line), and with cancerous colonic tissue (red line). d) Resonant frequency shift as a function of  $h_{\text{tissue}}$  for healthy (black dots) and cancerous tissue (red dots).

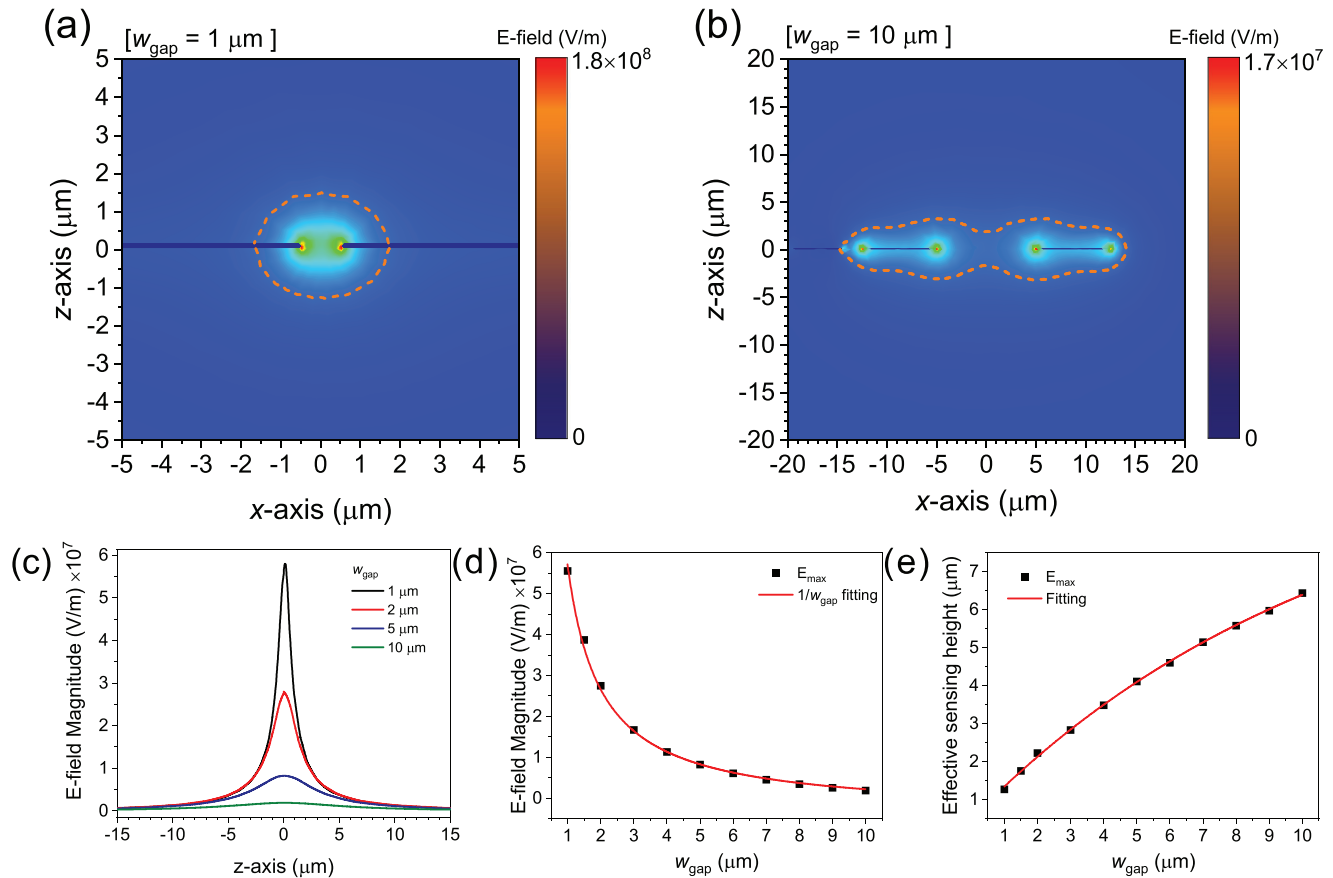


**Figure 3.** Electric field distribution near the SRR when a)  $w_{\text{gap}} = 1 \mu\text{m}$ , b)  $w_{\text{gap}} = 10 \mu\text{m}$ . c) Electric field magnitude at the centre of the gap along the  $z$ -axis, d) Maximum electric field magnitude (at  $z = 0 \mu\text{m}$ ) as a function of  $w_{\text{gap}}$ , e) Effective sensing height as a function of  $w_{\text{gap}}$ .

In **Figure 4**, we performed imaging of the colonic tissue model (Tissue model III) using the SRR integrated PGL with  $w_{\text{gap}} = 4 \mu\text{m}$ . From a practical point of view, the SRR integrated PGL should be covered by a protective dielectric layer for durability, and reusability. Therefore, we added a polyimide (PI) layer as a protective layer to the SRR integrated PGL as PI is biocompatible<sup>[18,19]</sup> and the thickness of the layer can be controlled by changing the spin-coating speed.<sup>[20]</sup> Figure 4a shows a perspective-view diagram of the PI covered SRR integrated PGL with Tissue model III on it. We note again that Tissue model III consists of healthy (outer area) and cancerous (inner circle area) colonic tissues. A cross-sectional view of the diagram along the  $z$ - $x$  plane is shown in Figure 4b. A  $1 \mu\text{m}$ -thick PI protective layer was used here to let the SRR distinguish the types of the colonic tissue on the protective layer with high sensitivity. The SRR becomes less sensitive to the permittivity difference between healthy and cancerous colonic tissues on the protective layer if the PI layer is too thick compared to the effective sensing height of the SRR as investigated in Figure 3, for example. To image Tissue model III with the PI covered SRR, Tissue model III was translated along the  $x$ - $y$  plane with a step of  $10 \mu\text{m}$  in the range of  $-100$  to  $100 \mu\text{m}$  in both the  $x$  and  $y$ -axis. The resonant frequency shift of the SRR was recorded at each  $x$ ,  $y$  position and then was plotted as a function of  $x$ ,  $y$  in Figure 4c. The imaging results revealed the structure of Tissue model III with excel-

lent agreement to its composition revealing the circular shape of the inner cancerous colonic tissue area and outer healthy colonic tissue area being clearly reconstructed allowing them to be distinguished from each other. We note that the spatial resolution of the SRR integrated on-chip probe can be adjusted by changing the gap width since the spatial resolution is determined by the volume of the electric field confinement in the capacitive gap area. However, the change in the effective sensing height should be also considered to optimise the sensitivity and the spatial resolution, depending on the specific application.

#### 4. Conclusion

We proposed a novel imaging technique using an SRR integrated with on-chip THz waveguides for CRC detection. Healthy and cancerous colonic tissues were modeled in the simulation by assigning permittivity and loss tangent from earlier experimental work.<sup>[2]</sup> Resonant frequency shift of the SRR was investigated with the loading of healthy (Tissue model I) and cancerous (Tissue model II) colonic tissues, finding they can be distinguished from each other by the resonant frequency shift. A study on electric field distribution and its confinement near the SRR showed that reducing  $w_{\text{gap}}$  increases the electric field magnitude in the gap area of the SRR, leading to greater sensitivity, while the effective sensing height decreases with

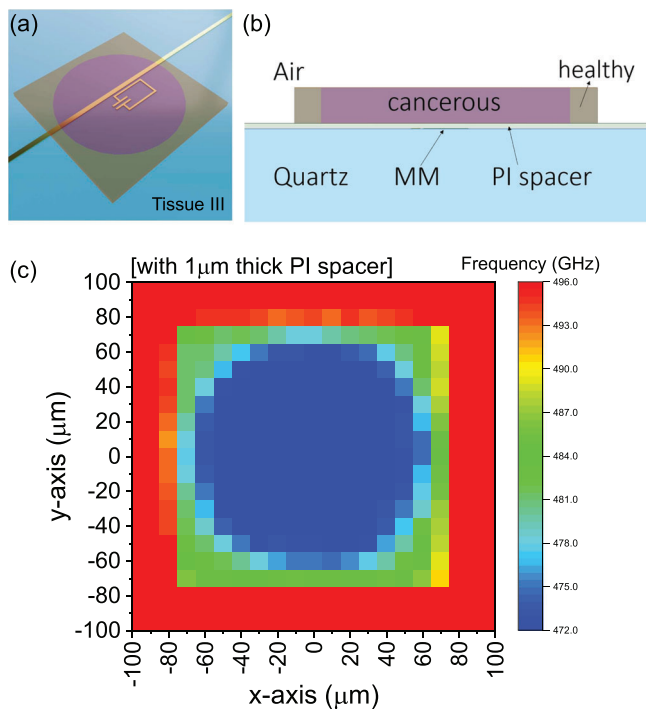


**Figure 4.** a) Perspective view and b) side view of a schematic of the SRR integrated PGL model with Tissue model III. c) 2D imaging results of Tissue model III using the PI covered SRR integrated PGL.

decreasing  $w_{\text{gap}}$ . Imaging of colonic tissue (Tissue model III) consisting of healthy and cancerous tissues was demonstrated and the imaging results were in excellent agreement with the known structure of Tissue model III. This approach for detecting CRC using SRR integrated on-chip waveguides can be combined with the existing and future colonoscopy techniques, potentially providing enhanced accuracy for diagnostics.

## Acknowledgements

The authors gratefully acknowledge funding from Engineering and Physical Sciences Research Council (EPSRC), grant number EP/V047914/1; The data associated with this paper is available from the University of Leeds at <https://doi.org/10.5518/1145>, reference number 21.

## Conflict of Interest

The authors declare no conflict of interest.

## Data Availability Statement

The data that support the findings of this study are openly available in University of Leeds at <https://doi.org/10.5518/1145>, reference number 21.

## Keywords

cancer detection, metamaterials, on-chip waveguide, split-ring resonator, terahertz imaging

Received: May 11, 2022

Revised: June 7, 2022

Published online:

- [1] J. Ferlay, M. Ervik, M. Colombet, L. Mery, M. Piñeros, A. Znaor, I. Soerjomataram, F. Bray, *Global Cancer Observatory: Cancer Today*, International Agency for Research on Cancer, Lyon, France **2020**, Available from: <https://gco.iarc.fr/today>, (accessed: May 2022).
- [2] C. B. Reid, A. Fitzgerald, G. Reese, R. Goldin, P. Tekkis, P. S. O'Kelly, E. Pickwell-Macpherson, A. P. Gibson, V. P. Wallace, *Phys. Med. Biol.* **2011**, *56*, 4333.
- [3] D. Lieberman, *Ann. Intern. Med.* **2004**, *141*, 401.
- [4] D. T. Simmons, G. C. Harewood, T. H. Baron, B. T. Petersen, K. K. Wang, F. Boyd-Enders, B. J. Ott, *Aliment. Pharmacol. Ther.* **2006**, *24*, 965.
- [5] A. Rahman, A. K. Rahman, B. Rao, *Biosens. Bioelectron.* **2016**, *82*, 64.
- [6] Z. D. Taylor, R. S. Singh, D. B. Bennett, P. Tewari, C. P. Kealey, N. Bajwa, M. O. Culjat, A. Stojadinovic, H. Lee, J. P. Hubschman, E. R. Brown, W. S. Grundfest, *IEEE Trans. Terahertz Sci. Technol.* **2011**, *1*, 201.
- [7] V. P. Wallace, A. J. Fitzgerald, S. Shankar, N. Flanagan, R. Pye, J. Cluff, D. D. Arnone, *Br. J. Dermatol., Suppl.* **2004**, *151*, 424.
- [8] J. Cunningham, M. B. Byrne, C. D. Wood, L. Dazhang, *Electron. Lett.* **2010**, *46*, S34.
- [9] S. J. Park, S. Zonetti, R. S. Parker-Jervis, J. Wu, C. D. Wood, L. H. Li, A. G. Davies, E. H. Linfield, O. Sydoruk, J. E. Cunningham, *Opt. Express* **2021**, *29*, 12958.
- [10] S. J. Park, J. Cunningham, *Sensors* **2020**, *20*, 4264.
- [11] S. K. Hwan, H. C. Sung, B. Roy, S. Kim, Y. H. Ahn, *Opt. Express* **2018**, *26*, 33575.
- [12] R. S. Parker-Jervis, S. J. Park, J. E. Cunningham, *J. Appl. Phys.* **2021**, *129*, 053101.
- [13] H. Lamela, E. Dadrasnia, D. M. Lee, S. Baik, M. B. Kuppam, F. Garet, J. L. Coutaz, presented at *Proc. SPIE*, San Diego, California, United States, **2012**.
- [14] K. Meng, S. J. Park, A. D. Burnett, T. Gill, C. D. Wood, M. Rosamond, L. H. Li, L. Chen, D. R. Bacon, J. R. Freeman, P. Dean, Y. H. Ahn, E. H. Linfield, A. G. Davies, J. E. Cunningham, *Opt. Express* **2019**, *27*, 23164.
- [15] J. F. O'Hara, R. Singh, I. Brener, E. Smirnova, J. Han, A. J. Taylor, W. Zhang, *Opt. Express* **2008**, *16*, 1786.
- [16] S. J. Park, S. A. N. Yoon, Y. H. Ahn, *J. Opt. Soc. Korea* **2016**, *20*, 628.
- [17] M. Beruete, I. Jáuregui-López, *Adv. Opt. Mater.* **2020**, *8*, 1900721.
- [18] C. P. Constantin, M. Aflori, R. F. Damian, R. D. Rusu, *Materials* **2019**, *12*, 3166.
- [19] F. Tjulkins, A. T. T. Nguyen, N. Hoivik, K. E. Aasmundtveit, E. Andreassen, L. Hoff, K. Imenes, presented at *Proc. Electron. Compon. Technol.*, Las Vegas, Nevada, United States, **2013**.
- [20] C. T. Pan, *Sens. Actuator, A* **2004**, *113*, 240.
- [21] S. J. Park, R. Tucker, E. Pickwell-MacPherson, J. E. Cunningham, *Dataset associated with "Design of a Split Ring Resonator Integrated with On-Chip Terahertz Waveguides for Colon Cancer Detection"*, **2022**, The data associated with this paper is available from the University of Leeds at <https://doi.org/10.5518/1145>.